Journal of Zhejiang University-SCIENCE A (Applied Physics & Engineering) *2024 25(3):223-237*
www.jzus.zju.edu.cn; www.springer.com/journal/11582
E-mail: jzus_a@zju.edu.cn

Research Article
https://doi.org/10.1631/jzus.A2300143

Check for updates

Non-uniform thermal behavior of single-layer spherical reticulated shell structures considering time-variant environmental factors: analysis and design

Wucheng XU[1,3,4], Xiaoqing ZHENG[2], Xuanhe ZHANG[1,3,4], Zhejie LAI[1], Yanbin SHEN[1,3,4]✉

[1]*College of Civil Engineering and Architecture, Zhejiang University, Hangzhou 310058, China*
[2]*Center for Balance Architecture, Zhejiang University, Hangzhou 310028, China*
[3]*Innovation Center of Yangtze River Delta, Zhejiang University, Jiaxing 314100, China*
[4]*Zhejiang Provincial Key Laboratory of Space Structures, Zhejiang University, Hangzhou 310058, China*

Abstract: Contrary to conventional design methods that assume uniform and slow temperature changes tied to atmospheric conditions, single-layer spherical reticulated shells undergo significant non-uniform and time-variant temperature variations due to dynamic environmental coupling. These differences can affect structural performance and pose safety risks. Here, a systematic numerical method was developed and applied to simulate long-term temperature variations in such a structure under real environmental conditions, revealing its non-uniform distribution characteristics and time-variant regularity. A simplified design method for non-uniform thermal loads, accounting for time-variant environmental factors, was theoretically derived and validated through experiments and simulations. The maximum deviation and mean error rate between calculated and tested results were 6.1 ℃ and 3.7%, respectively. Calculated temperature fields aligned with simulated ones, with deviations under 6.0 ℃. Using the design method, non-uniform thermal effects of the structure are analyzed. Maximum member stress and nodal displacement under non-uniform thermal loads reached 119.3 MPa and 19.7 mm, representing increases of 167.5% and 169.9%, respectively, compared to uniform thermal loads. The impacts of healing construction time on non-uniform thermal effects were evaluated, resulting in construction recommendations. The methodologies and conclusions presented here can serve as valuable references for the thermal design, construction, and control of single-layer spherical reticulated shells or similar structures.

Key words: Non-uniform temperature field; Non-uniform thermal load; Non-uniform thermal effect; Single-layer spherical reticulated shell; Time-variant environmental factor

1 Introduction

Because of its robust mechanical properties and efficient material strength utilization, the single-layer spherical reticulated shell is extensively used in large infrastructures. The temperature of such a structure varies significantly non-uniformly throughout its life-cycle, including the construction and service periods, due to the dynamic interplay of various environmental factors like solar radiation, wind, and atmospheric temperature (AT). Previous experiments have revealed that under intense solar radiation, the temperature of steel components can significantly exceed ATs, with the disparity even surpassing 30 ℃ (Liu and Chen, 2016). Traditional design methodologies often assume that temperature changes in a building structure occur uniformly and progressively (MOHURD, 2010, 2012). However, this simplification can result in discrepancies between the design and practical conditions, and neglecting the non-uniformity and time-variability of temperature changes may pose significant safety hazards. Therefore, it is vital to study the changing patterns and distribution characteristics of non-uniform temperature variations. We see that it is necessary to devise an efficient and systematic method for designing non-uniform thermal loads that would account for

✉ Yanbin SHEN, ybshen@zju.edu.cn
Wucheng XU, https://orcid.org/0000-0002-3816-9421
Yanbin SHEN, https://orcid.org/0000-0002-2148-9138

Received Mar. 18, 2023; Revision accepted June 23, 2023; Crosschecked Jan. 18, 2024

multiple environmental factors, and apply it in structural thermal analysis.

Previous structural engineering studies on non-uniform thermal behavior have focused on bridges (Zhou and Sun, 2019), components (Liu et al., 2012a), and radio telescopes (Greve and Kaercher, 2009). Many elements such as radiation, AT, and convective heat transfer, complicate the temperature field within bridge structures (Xia et al., 2013). Significant thermal effects, potentially causing hidden safety issues, can be instigated by the high time-variance and non-uniformity of a bridge's temperature field (Kim et al., 2015). Ascertaining the distribution and trend of temperature changes in bridges plays a pivotal role in guaranteeing their safety. In steel components, the temperature is uniform longitudinally and across thickness, but displays clear non-uniformity cross-sectionally (Liu et al., 2012b). Experiments have shown that under specific conditions, the maximum thermal stresses of steel components can reach 67 and 58 MPa under rigid and hinged constraints, respectively (Chen et al., 2017b). The uneven temperature distribution frequently results in pronounced thermal effects on steel components, which is a fact corroborated by extensive research. Non-uniform thermal deformation, caused by factors such as solar radiation and wind, can alter a telescope's geometric shape during operation from its original design (Chen et al., 2017a). This discrepancy can negatively impact the accuracy of reflector surface precision and pointing accuracy, thus leading to observational errors, as demonstrated in the research involving the Five-hundred-meter Aperture Spherical Telescope (Fan et al., 2009), Shanghai 65 m Radio Telescope (Qian et al., 2016), and the IRAM-30 m Telescope (Greve and Bremer, 2010). The thermal analysis and control frequently constitute a critical aspect of telescope design.

As structures with high static indeterminacy, spatial structures exhibit considerable sensitivity to temperature variations (Chen et al., 2021; Xu et al., 2021). In the past, numerous scientists have conducted studies on various actual spatial structure projects, and investigated changes in their temperature during construction and service periods (Xu et al., 2020). These projects include the Tien Rice Cube, China (Liu et al., 2015), Yujiabu Railway Station, China (Zhao et al., 2017), Xi'an Silk Road International Convention and Exhibition Center, China (Chen et al., 2020), and Beijing Daxing International Airport, China (Zhou et al., 2020). The research findings indicate that during construction, spatial structures directly exposed to solar radiation exhibit noticeably non-uniform temperature field distributions due to the coupling effects of various dynamic environmental factors, and that during service, as a result of factors such as transmission properties of roofing materials, thermal conduction between the roof and structure, and temperature box effect, spatial structures may experience even more complex temperature changes and distribution. Thus, the design of spatial structures should take into account the non-uniformity of temperature changes. However, previous research usually analyzed the non-uniform temperature change characteristics of one specific engineering and its impact on structural performance through monitoring and simulation data. As of yet, no published paper has touched on the design of non-uniform thermal loads in spatial structures. The work in this paper is intended to fill this research gap, and specifically, to provide a simplified design methodology for the non-uniform thermal loads of single-layer spherical reticulated shells, which is a common form of spatial structure.

This study employs a systematic numerical method to model the temperature fields of a single-layer spherical reticulated shell, taking into account dynamic environmental factors and shadow changes. The non-uniform distribution and time-variant patterns are revealed through simulation. A theoretically-derived, and experimentally- and numerically-validated design method for non-uniform thermal loads is proposed. The structure's non-uniform thermal effects and the impact of healing construction time on these effects are analyzed, resulting in specific construction recommendations.

2 Analysis of non-uniform temperature field

2.1 Numerical simulation method

In this study, a thermal analysis strategy for single-layer spherical reticulated shells was applied. It represents the single-layer spherical reticulated shell using a spherical steel skin of the same size and material, equating the steel component's temperature with that of the steel skin at the same position. Similar approaches have been used in previous studies (Liu et al., 2014,

2015). We used a single-layer spherical reticulated shell of Q345 steel with a span of 30 m and rise of 12 m, built in Beijing, China, as the study object. ANSYS was applied for thermal analysis, and Shell57, Link31, and Surf152 elements were used to simulate the heat conduction, convection, and radiation. Fig. 1 presents the simulation process of the temperature field. National Aeronautics and Space Administration (NASA)-provided data on AT, solar radiation intensity (SRI), and wind speed (WS) were adopted as the environmental boundary conditions for the process (GMAO, 2015).

2.2 Shadow analysis algorithm

For precise temperature field simulation under solar radiation, it is crucial to identify shaded regions on the steel skin. In this study, a shadow analysis algorithm was proposed to address this, which can be described as follows:

Step 1: A global coordinate system, *OXYZ*, is created using geographic and geometric data. The *XOY* plane is parallel to the ground and the *X*, *Y*, and *Z* axes point to the west, south, and sky.

Step 2: Solar altitude and azimuth angles are calculated using Eqs. (1) and (2); a local coordinate system, *oxyz*, is defined (Fig. 2), with Eq. (3) outlining its conversion from *OXYZ*.

$$\sin\alpha_s=\sin\phi\sin\delta+\cos\phi\cos\delta\cos\psi, \tag{1}$$

$$\cos\beta_s=\frac{\sin\delta-\sin\alpha_s\sin\phi}{\cos\alpha_s\cos\phi}, \tag{2}$$

$$\begin{bmatrix}x\\y\\z\end{bmatrix}=\begin{bmatrix}\cos A_s & 0 & -\sin A_s\\0 & 1 & 0\\\sin A_s & 0 & \cos A_s\end{bmatrix}\cdot\begin{bmatrix}\cos B_s & \sin B_s & 0\\-\sin B_s & \cos B_s & 0\\0 & 0 & 1\end{bmatrix}\cdot\begin{bmatrix}X\\Y\\Z\end{bmatrix}, \tag{3}$$

where α_s and β_s are the solar altitude and azimuth angles, ϕ, δ, and ψ are the geographic latitude, obliquity of the ecliptic, and solar hour angle, respectively, and angles A_s=90°−α_s and B_s=270°−β_s.

Step 3: Triangular skin elements are projected onto the *xoy* plane (utilizing the sunlight direction) with vertex and barycenter coordinates calculated for each element.

Step 4: Determine whether it is daytime (α_s>0) or nighttime (α_s<0). If it is nighttime, all elements are shaded; if not, continue to the next step.

Step 5: Take one element as the study object. In the *xoy* plane, if the element's barycenter is located within other elements, these are selected for further analysis; otherwise, it is a sunlit element.

Step 6: Under the *oxyz* system, the study object's relationship to the selected elements is evaluated in terms of their *z*-values. If the study object's *z*-value is the highest, it is a sunlit element; otherwise, it is shaded.

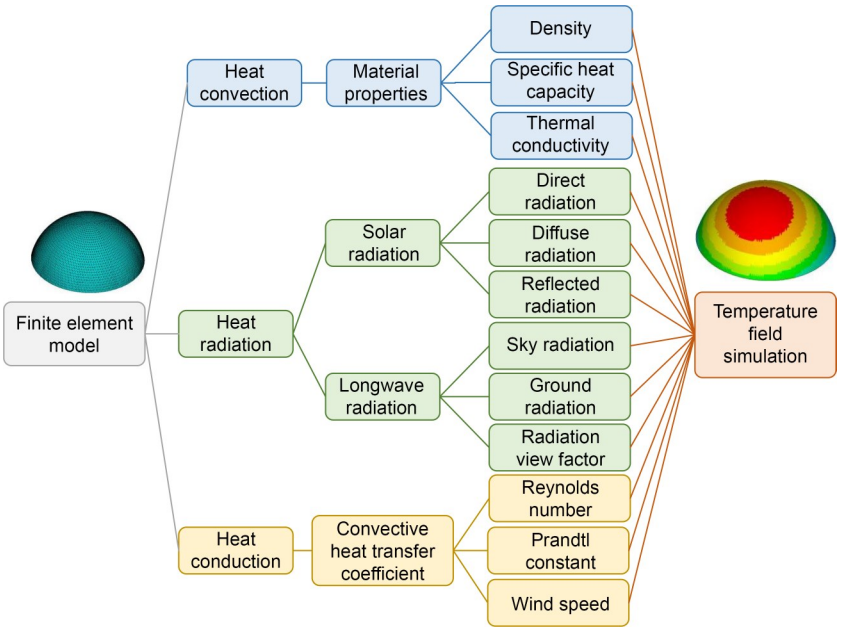

Fig. 1 Simulation process of the temperature field

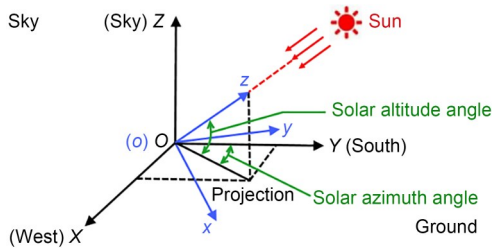

Fig. 2 Conversion relationship between *OXYZ* and *oxyz*

Step 7: Steps 4–6 are repeated for all elements to decide whether they are sunlit or shaded, thus identifying the sunlit and shaded regions.

The shadow distribution variations on important solar cycle dates are depicted in Fig. 3. Red and blue elements denote sunlit and shaded elements, respectively. The western, northern, and eastern elements are shaded during morning, noon, and afternoon, respectively. At the summer solstice, with the sun closest to the structure, daylight is the longest and shadows are the smallest; at the winter solstice, when the sun is the farthest, daylight is the shortest and shadows are the largest; during the spring and autumn equinoxes, shadow changes are the same. The analysis accurately mirrors real-world shadow effects, affirming the algorithm's accuracy.

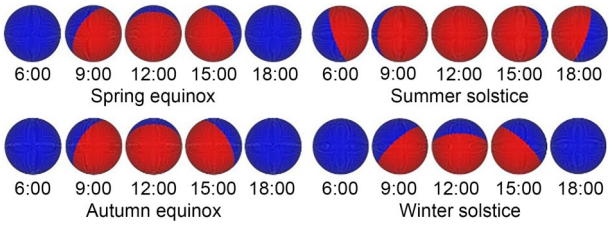

Fig. 3 Shadow distribution variations on important solar cycle dates. References to color refer to the online version of this figure

2.3 Seasonal temperature variation and distribution

The studied structure's temperature was simulated throughout the entire year by utilizing the environmental boundary parameters of Beijing in 2021. Fig. 4 shows the variation curves for several temperature metrics: the daily maximum and minimum of the structural temperature field (ST_{max} and ST_{min}) and those of ATs (AT_{max} and AT_{min}). ST_{max} peaks at 69.1 °C on July 7 and ST_{min} hits a low of −19.5 °C on Jan. 17, while the maximum of AT_{max} and minimum of AT_{min} reach 37.6 and −18.9 °C on June 19 and Jan. 17,

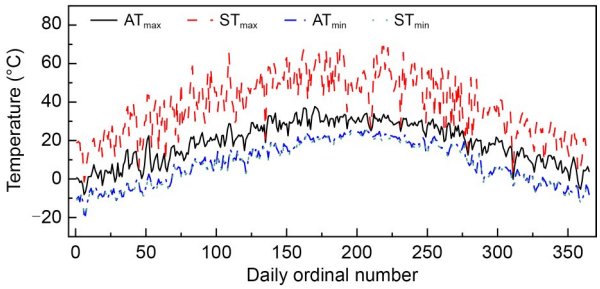

Fig. 4 Variation curves of structural and atmospheric temperatures

respectively. The structural temperature exhibits the annual range and maximal daily range of 88.6 and 55.3 °C, which are 1.6 and 2.5 times higher than those of the AT. The variation trends in structural temperatures and ATs are similar. However, the daily maximum of structural temperatures is typically much greater than that of ATs. The findings suggest that due to the structural temperature's non-uniformity and the fact that it usually surpasses the AT, relying only on the latter for thermal load design may not be sufficient.

Tables 1 and 2 itemize the temperature field information, namely ST_{max} and ST_{min}, temperature range (TR), AT, SRI, and WS, at the moments corresponding to the top 10 highest ST_{max} and lowest ST_{min}, respectively. The moments corresponding to the top 10 highest ST_{max} are usually around noon in the summer, when the temperature field information shows the following features:

1. The temperature field distribution is non-uniform, with the temperature differences all exceeding 32.0 °C.

Table 1 Temperature field information for the top 10 highest ST_{max}

Time	ST_{max} (°C)	TR (°C)	AT (°C)	SRI (W/m^2)	WS (m/s)
12:00, July 7	69.1	37.0	30.2	853.8	0.3
13:00, Aug. 7	68.8	35.0	32.6	854.7	0.8
14:00, Aug. 6	68.7	35.7	31.3	770.0	0.3
13:00, July 8	68.5	34.7	32.4	871.4	1.0
14:00, Aug. 10	68.2	33.9	32.9	801.9	0.7
14:00, June 27	67.5	32.3	33.0	802.5	1.0
12:00, June 11	67.1	32.4	33.0	896.0	1.8
14:00, July 9	66.8	33.2	31.7	816.1	1.0
13:00, Aug. 21	65.7	33.5	31.4	802.6	0.7
13:00, July 5	65.6	32.1	32.1	754.3	0.6

Table 2 Temperature field information for the top 10 lowest ST_{min}

Time	ST_{min} (℃)	TR (℃)	AT (℃)	SRI (W/m²)	WS (m/s)
7:00, Jan. 7	−19.5	0.2	−18.9	0.0	4.0
0:00, Jan. 6	−19.0	0.2	−18.4	0.0	5.3
8:00, Jan. 8	−14.5	0.1	−13.5	5.4	1.3
8:00, Jan. 3	−12.5	0.3	−11.7	5.0	1.7
8:00, Dec. 25	−12.3	0.2	−11.7	6.2	4.5
8:00, Jan. 5	−12.0	0.2	−11.4	5.3	2.7
7:00, Dec. 26	−11.9	0.2	−10.8	0.0	2.1
7:00, Jan. 29	−11.7	0.3	−10.9	0.0	1.8
8:00, Jan. 9	−11.0	0.3	−10.1	5.4	2.5
8:00, Jan. 1	−10.8	0.3	−10.2	5.1	2.3

2. The temperature field is higher than the AT, with ST_{max} averaging 35.5 ℃ higher.

3. Atmospheric temperatures are high, all above 30.0 ℃; solar radiations are intense, with all intensities above 750.0 W/m²; WSs are minimal, averaging only 0.8 m/s.

Conversely, the moments corresponding to the top 10 lowest ST_{min} typically fall around early morning in the winter, when the temperature field information exhibits the following characteristics:

1. The temperature field distribution is uniform, with no TR higher than 0.3 ℃.

2. The temperature field is below the AT, with ST_{min} averaging 0.8 ℃ lower.

3. Atmospheric temperatures are low, all below −10.0 ℃; there is no or minimal solar radiation, all under 7.0 W/m² in intensity; WSs are not insignificant, reaching an average of 2.8 m/s.

In general, high structural temperatures occur mainly at noon in summer with high ATs, strong solar radiation, and weak winds, when the temperature field is non-uniform and much higher than the AT; low structural temperatures occur mainly in early morning in winter with low ATs, no or minimal solar radiation, and strong winds, when the temperature field is uniform and slightly lower than the AT.

2.4 Daily temperature variation and distribution

Figs. 5 and 6 illustrate the time-varying curves of the maximum (T_{max}), minimum (T_{min}), and standard deviation (T_{sd}) of temperature fields on the typical days of Jan. 7 and July 7, when the annual minimum and maximum structural temperatures are observed, alongside the AT, SRI, and WS. At nighttime, T_{max} and T_{min} are nearly equal and marginally below the AT; in the daytime, T_{min} is slightly above the AT, while T_{max} is significantly greater than AT. Peaks of T_{max} are observed at 2.3 and 69.1 ℃ at 14:00 on Jan. 7 and 12:00 on July 7, respectively, which are 9.7 and 38.9 ℃ above the AT, respectively. This indicates that the structural temperature fields are uniform at nighttime and non-uniform in the daytime. During the daytime, the mean values of SRI and WS are 277.7 W/m² and 3.6 m/s on Jan. 7 (with an average T_{sd} of 2.0 ℃), and 412.7 W/m² and 1.3 m/s on July 7 (with an average T_{sd} of 5.4 ℃). T_{sd} grows with enhanced solar radiation when WS is comparable, and conversely, diminishes as WS increases with consistent SRI. This suggests that the non-uniformity of temperature field distribution depends on environmental boundary conditions, exhibiting a positive correlation with SRI and a negative one with WS.

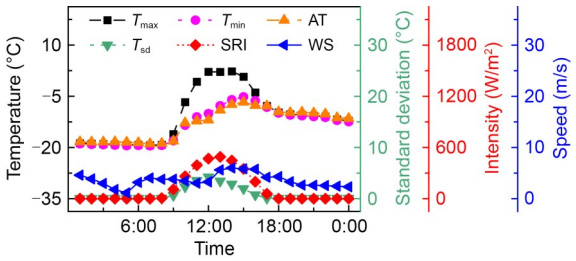

Fig. 5 Simulated temperature fields on Jan. 7

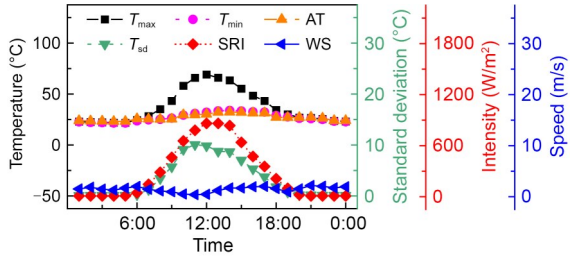

Fig. 6 Simulated temperature fields on July 7

Figs. 7 and 8 show the simulated temperature fields on typical days and also demonstrate the sun's position relative to the structure. The variation rules of temperature field distribution are consistent over these two days, shifting as the sun rises and sets. The temperature field distribution reveals a distinct gradient, with the highest temperatures in areas perpendicular to sunlight and the lowest in shaded regions, which is

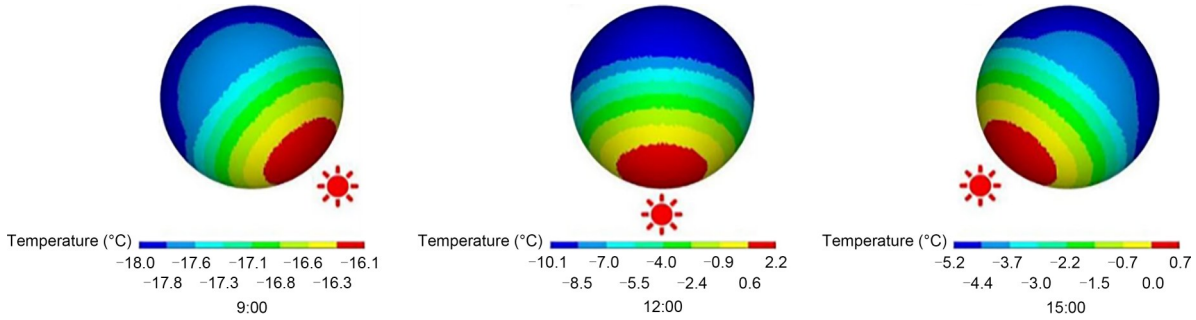

Fig. 7 Simulated temperature fields on Jan. 7

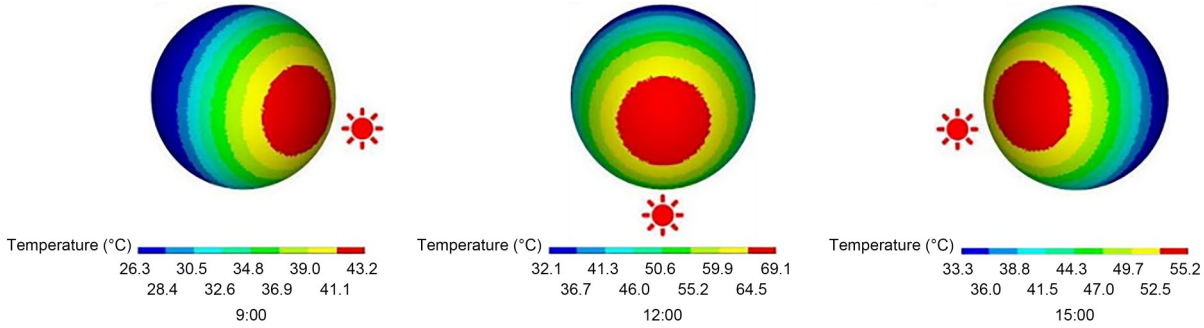

Fig. 8 Simulated temperature fields on July 7

a pattern attributable to uneven absorption of solar radiation by the structure's surface. While the SRI and WS determine the degree of non-uniformity in temperature field distribution, such as temperature field differences of 12.3 ℃ on Jan. 7 and 37.0 ℃ on July 7 at 12:00, the temperature field distribution pattern relies solely on the sun's position relative to the structure.

3 Design of non-uniform thermal load

3.1 Theoretical design method

Numerical analysis revealed that the temperature field of the single-layer spherical reticulated shell, influenced by environmental factors, is significantly non-uniform and above the AT. This emphasizes the importance of considering these factors in thermal load design. As such, this study proposes a simplified thermal load design method that accounts for environmental factors.

Conceptualizing the spherical steel skin as numerous infinitesimal plane steel plates allows us to determine the structural temperature field by calculating the temperature of the plates. The following section outlines the calculation process for any given plane steel plate.

The general form of the transient heat conduction differential equation for a steel plate exposed to the natural environment is expressed as

$$\frac{\lambda}{\rho c}\left(\frac{\partial^2 T}{\partial x^2}+\frac{\partial^2 T}{\partial y^2}+\frac{\partial^2 T}{\partial z^2}\right)=\frac{\partial T}{\partial t}, \tag{4}$$

where λ, ρ, and c are the thermal conductivity, density, and specific heat capacity of the steel plate, respectively, T is the temperature of the steel plate, x, y, and z are coordinates of the steel plate, and t is the time.

Addressing the temperature problem requires solving the heat conduction differential equation via initial and boundary conditions. The initial condition defines the steel plate's initial temperature, while the boundary condition outlines the heat exchange at the plate's boundary, as described by:

$$\lambda\frac{\partial T}{\partial n}\bigg|_{\Gamma}=q(t), \tag{5}$$

where Γ is the boundary of the steel plate, n is the exterior normal direction of Γ, and q is the heat flux flowing into the steel plate from outside.

Due to steel's high thermal conductivity, the temperature gradient across the plate section is negligible,

making the heat flux from the interior to the surface zero. Hence, Eq. (5) is expressed as

$$\lambda \frac{\partial T}{\partial n}\bigg|_{\Gamma} = 0. \tag{6}$$

On the plate surface, the heat flow loads that contain the heat fluxes of convective heat transfer (q_c), solar radiation (q_s), and longwave radiation (q_l) are reflected as

$$q = q_c + q_s + q_l. \tag{7}$$

Convective heat transfer between the plate surface and flowing air is computed by

$$q_c = h_c(T_a - T), \tag{8}$$

where h_c is the convective heat transfer coefficient and T_a is the atmospheric temperature.

Solar radiation absorbed by the plate surface is calculated by

$$q_s = \alpha\left(I_b \omega \cos\theta + I_d F_{ws} + I_t R_g F_{wg}\right), \tag{9}$$

where α is the solar radiation absorption coefficient of the steel plate's surface; I_b and I_d are the direct and diffuse radiation intensities, respectively; $I_t = I_b + I_d$ is the total radiation intensity; ω and θ are the daylight coefficient and incidence angle, respectively; F_{ws} and F_{wg} are the sky and ground angle factors, respectively; R_g is the surface albedo. ω, θ, F_{ws}, and F_{wg} are computed by

$$\omega = \begin{cases} 0, & \cos\theta \leqslant 0, \\ 1, & \cos\theta > 0, \end{cases} \tag{10}$$

$$\cos\theta = \cos\alpha_s \cos\gamma \sin\varphi + \sin\alpha_s \cos\varphi, \tag{11}$$

$$F_{ws} = 0.5(1 + \cos\varphi), \tag{12}$$

$$F_{wg} = 0.5(1 - \cos\varphi), \tag{13}$$

where γ is the surface solar azimuth and φ is the tilt angle.

Longwave radiation absorbed by the plate surface is calculated by

$$q_l = q_{l,s} + q_{l,g}, \tag{14}$$

where $q_{l,s}$ and $q_{l,g}$ are the heat fluxes of sky and ground longwave radiations, respectively, which are calculated by

$$q_{l,s} = \varepsilon_f \sigma (T_s^4 - T^4) F_{ws}, \tag{15}$$

$$q_{l,g} = \varepsilon_f \sigma \left(T_g^4 - T^4\right) F_{wg}, \tag{16}$$

where ε_f and σ are the steel plate surface's emissivity and Stefan-Boltzmann constant, and T_s and T_g are the sky and ground temperatures, respectively.

The temperature of any steel plate can be calculated using the equations above. Taking several steel plates from the structure as the interpolation points, we adopted biharmonic spline interpolation to determine the temperature field (Deng and Tang, 2011).

3.2 Experimental verification

Experiments were conducted to test the accuracy and reliability of the design method. Test platform was a rotatable tripod installed with a steel plate, and nine platforms (at various angles) to simulate steel plates with different orientations within the structure. Real-time environmental boundary conditions and steel plate temperatures are monitored using test equipment, as shown in Fig. 9 and detailed in Table 3. Test site was on a well-ventilated and sunny rooftop, and the test period covered 15 d from July 16 to July 30, 2021. Five types of steel plates with different coating colors were used, as listed in Table 4 (Liu and Chen, 2016).

Figs. 10–13 presents the comparison between the measured and calculated temperatures of some steel plates on July 19, when the highest sample temperature was observed. The measured and calculated results followed consistent trends. At nighttime, measured and calculated temperatures were nearly identical, with a discrepancy of less than 1.0 °C, while during the daytime, measured temperatures lagged slightly behind calculated ones, with calculated temperatures being

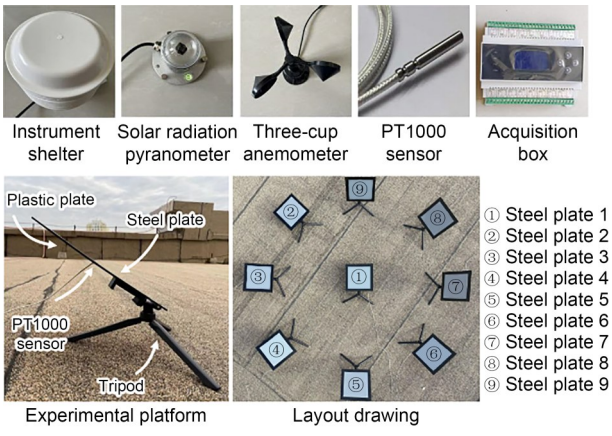

Fig. 9 Test equipment and experimental platforms

Table 3 List of test equipment

Test content	Equipment	Test range	Precision
AT	Instrument shelter	−40.0–80.0 °C	0.5 °C
Solar radiation	Solar radiation pyranometer	0–1500 W/m^2	1 W/m^2
WS	Three-cup anemometer	0.00–30.00 m/s	0.01 m/s
Steel plate temperature	PT1000 sensor	−50.00–200.00 °C	0.15 °C
Data collection	Acquisition box	32 channels	–

Table 4 Test information for the five types of steel plates

No.	Finish coating color (RAL)	Solar radiation absorption coefficient	Experimental period
1	Red (3020)	0.66	July 16–18
2	Gray (7045)	0.75	July 19–21
3	Green (6017)	0.68	July 22–24
4	Yellow (1033)	0.45	July 25–27
5	White (9003)	0.32	July 28–30

RAL is a globally recognized color matching system, originally developed in Germany, which provides a standardized palette of colors for use in various industries such as manufacturing, architecture, and design

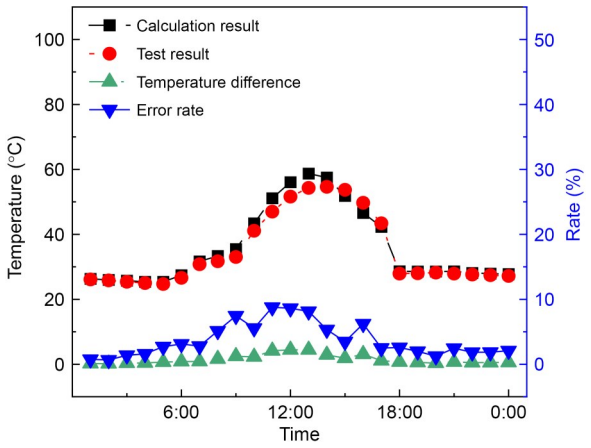

Fig. 10 Temperatures of steel plate 3 on July 19

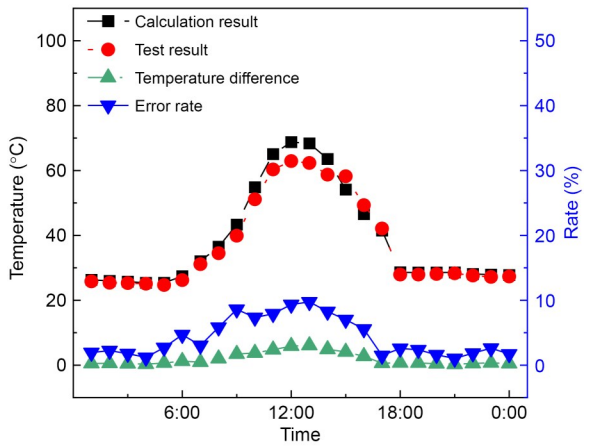

Fig. 11 Temperatures of steel plate 5 on July 19

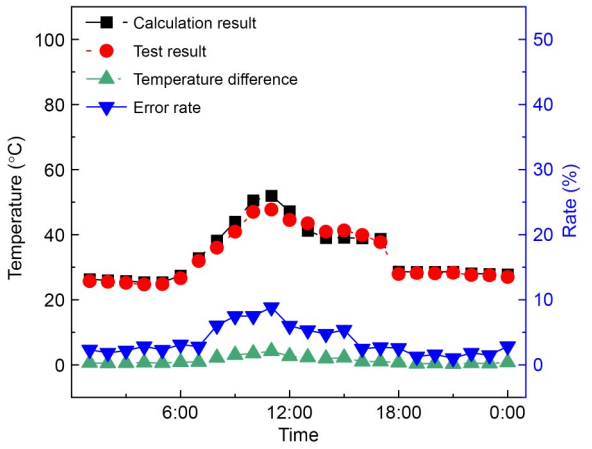

Fig. 12 Temperatures of steel plate 7 on July 19

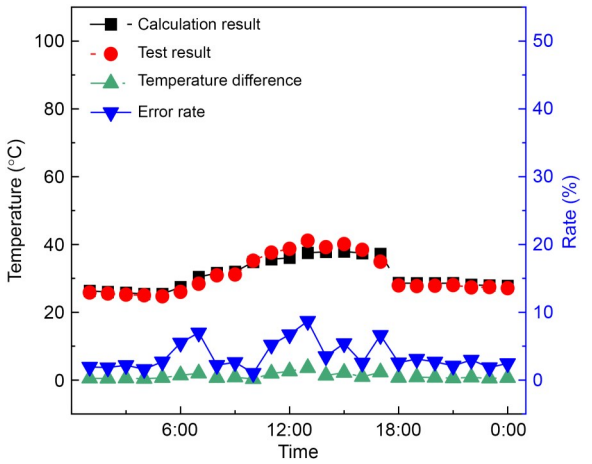

Fig. 13 Temperatures of steel plate 9 on July 19

marginally higher and error rising with temperature. For the four steel plates, the maximum temperature differences between measurements and calculations were 4.4, 6.1, 4.2, and 4.6 °C, with peak error rates of 8.8%, 9.7%, 8.8%, and 8.7%, respectively. The error mainly stemmed from calculating temperatures at thermal equilibrium, while tests measured transient temperatures. Based on the comparison of measured and calculated results, Fig. 14 displays the maximum and root mean square (RMS) of temperature differences

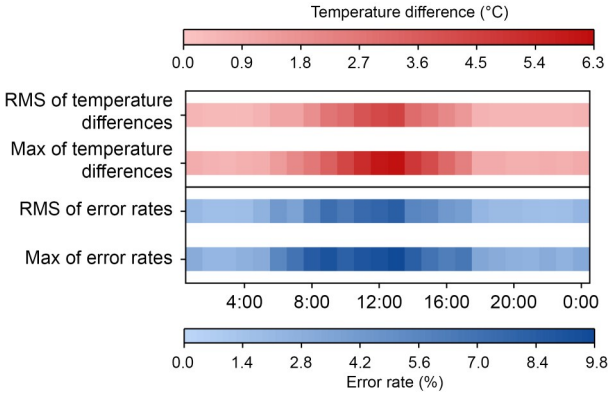

Fig. 14 Temperature differences and error rates between measured and calculated results on July 19. Max: maximum

and error rates for all tested steel plates on July 19. At 13:00, the maximum and RMS of temperature differences reached peaks of 6.1 and 4.4 °C, and those of error rates achieved peaks of 9.7% and 8.3%, respectively. The mean values of temperature differences and error rates throughout the day for these steel plates were only 1.5 °C and 3.7%. In summary, the calculated results were in agreement with measured results, which verified the accuracy and reliability of the design method.

3.3 Numerical verification

The calculated temperature fields on the typical days are shown in Figs. 15 and 16. Figs. 17 and 18 presents the variation curves of the maximum and minimum of the simulated and calculated temperature fields on the typical days. The simulated and calculated temperature fields shared distribution patterns, and the calculated results accurately echoed the impact of solar motion. For the six moments, the calculated maximums exceeded simulated ones by 1.1–5.9 °C, and minimums were 0.8–1.8 °C higher, with greater calculation error observed in the summer temperature field compared to the winter one. The calculated results have the same pattern of variation as the simulations, with slightly higher values for the former; the difference between the two is relatively small at nighttime and more significant in the daytime. On Jan. 7, the simulated maximum and minimum were higher than the calculated ones by an average of 0.6 and 0.8 °C at nighttime, and by 2.1 and 0.8 °C in the daytime, respectively; the differences between simulated and calculated maximums, and simulated and calculated minimums peaked at 2.1 and 2.3 °C, respectively, at 10:00. On July 7, the calculated maximums and minimums were, on average, higher than the simulated ones by 0.8 and 1.2 °C at nighttime, and by 3.1 and 1.7 °C in the daytime, respectively; the largest differences between simulated and calculated maximums, and simulated and calculated minimums were 5.9 and 3.3 °C at 12:00 and 10:00, respectively. In general, the consistency between simulated and calculated results confirmed the precision and reliability of the design method.

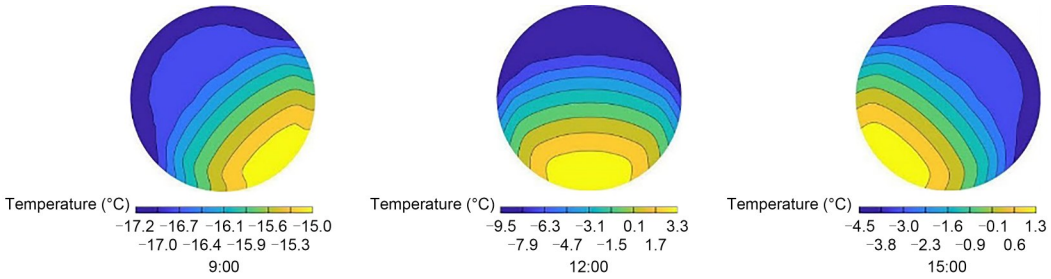

Fig. 15 Calculated temperature fields on Jan. 7

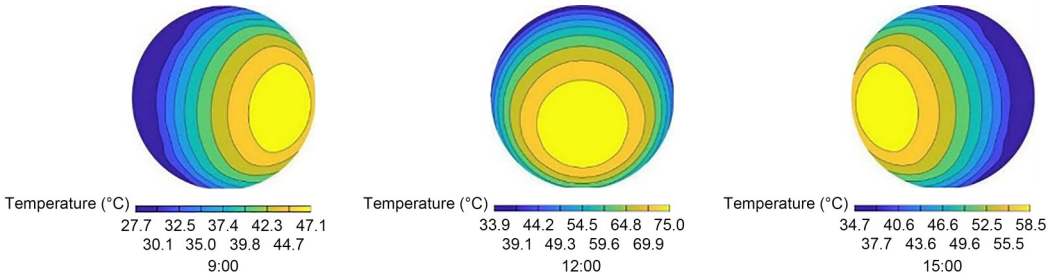

Fig. 16 Calculated temperature fields on July 7

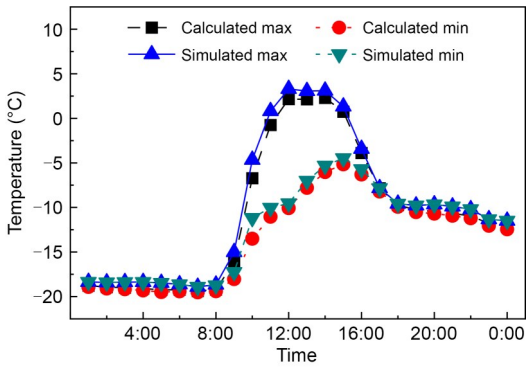

Fig. 17 Simulated and calculated results of temperature fields on Jan. 7. Min: minimum

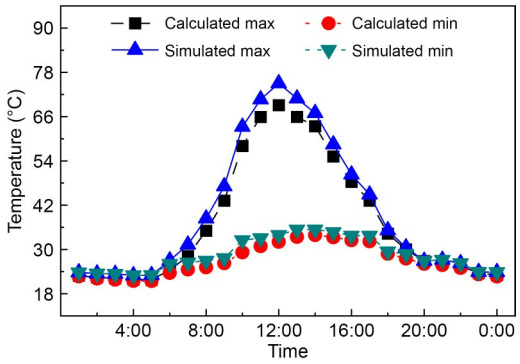

Fig. 18 Simulated and calculated results of temperature fields on July 7

3.4 Application instruction

Temperature load design entails computing the peak and trough temperature fields, which correspond to the maximum and minimum temperatures experienced by the structure in service. Additionally, the healing temperature field, representing the structure's temperature during its creation, must be determined. Based on the analysis in Section 2.4, we set the environmental boundary conditions of the peak temperature field to the maximum AT, the strongest solar radiation, and zero wind; the trough temperature field was uniformly set to 1 °C below the minimum AT. Temperature-rise and temperature-drop loads can be designed by

$$\Delta T_r = T_p - T_h, \tag{17}$$

$$\Delta T_d = T_t - T_h, \tag{18}$$

where ΔT_r and ΔT_d are the temperature-rise and temperature-drop loads, and T_p, T_t, and T_h are the peak, trough, and healing temperature fields, respectively.

Taking the structure under study as an example, the roof was designated as either glass or opaque, with a solar radiation transmittance of 0.7 or 0. Healing times were set for 9:00, 12:00, and 15:00 on Mar. 1, 2021, which was the date when the AT would approach its annual midpoint. The application of the design method was illustrated by the six cases. The meteorological data (1922–2021) indicated that Beijing's AT ranged from 42.6 to −27.4 °C. Using the Hottel model (Hottel, 1976), Beijing's strongest solar radiation was identified at 12:00 on June 18, with direct and diffuse intensities of 794.1 and 110.6 W/m^2, respectively. We utilized this information to calculate the peak, trough, and healing temperature fields. The non-uniform thermal loads designed for healing times on Mar. 1 are shown in Figs. 19 and 20. For the same healing time, temperature-drop loads were consistent across roof types, but the temperature-rise load was greater for glass roofs compared to opaque ones due to differing peak temperature fields. With varying healing times, thermal load distributions and ranges significantly differed due to diverse healing temperature fields. The glass roof experienced more adverse temperature-rise loads than the opaque roof. In summary, the non-uniform thermal load distribution aptly depicts the temporal variation of the temperature field across the lifecycle, encompassing both construction and service phases.

4 Analysis of non-uniform thermal effect

4.1 Uniform and non-uniform thermal effects

The above analysis reveals that the temperature variation in a single-layer spherical reticulated shell is non-uniform and time-variant, which is an aspect overlooked in traditional design methods that regard it as a uniform and slow process driven by AT. To assess the impact of uniform and non-uniform thermal loads on the structure, we conducted a comparative analysis using both the conventional method for uniform loads and the novel method proposed here for non-uniform loads, as outlined in Table 5. In line with the aforementioned sections, a single-layer spherical reticulated shell, as shown in Fig. 21, constructed in Beijing was designed for structural analysis, and Q345 steel pipes (Φ180 mm×6 mm) were used as principal members, with the structure supported by 16 concrete columns. The structure was assumed to be exposed to natural

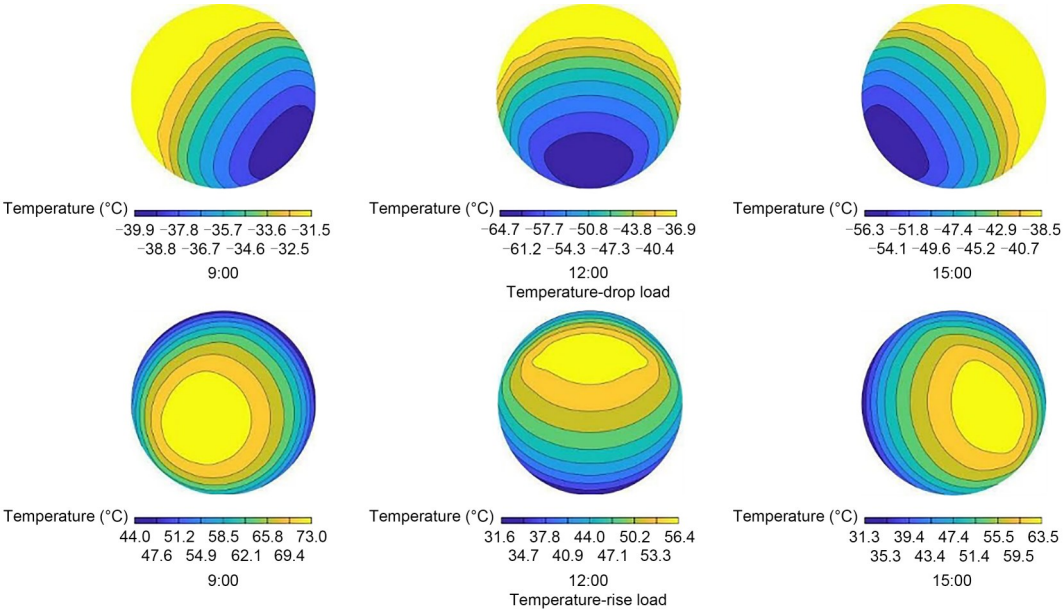

Fig. 19 Non-uniform thermal loads for glass roof on Mar. 1

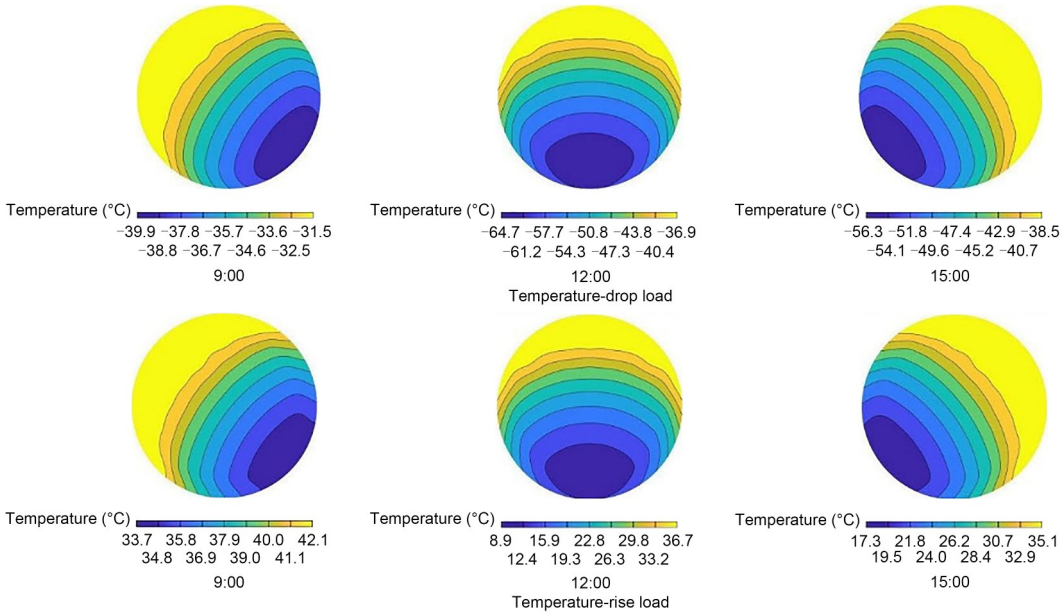

Fig. 20 Non-uniform thermal loads for opaque roof on Mar. 1

conditions during healing and covered with an opaque roof in service. ANSYS is used to analyze the structural thermal effects under the given loads, using Beam188 elements to simulate members, and bottom supports are modeled as hinged joints, with the created finite element model displayed in Fig. 21.

The uniform and non-uniform thermal effects were analyzed at healing times of 9:00, 12:00, and 15:00, for Mar. 1, 2021, and the results are summarized in Table 6. Under uniform thermal loads, the maximum

Table 5 Definition for four thermal loads

Load type	Definition
UTRL	$(T^{\mathrm{a}}_{\max}-T^{\mathrm{a}}_{\min})/2$
UTDL	$(T^{\mathrm{a}}_{\min}-T^{\mathrm{a}}_{\max})/2$
NTRL	$T_{\mathrm{p}}-T_{\mathrm{h}}$
NTDL	$T_{\mathrm{t}}-T_{\mathrm{h}}$

UTRL, UTDL, NTRL, and NTDL are the uniform temperature-rise load, uniform temperature-drop load, non-uniform temperature-rise load, and non-uniform temperature-drop load, respectively; $T^{\mathrm{a}}_{\max}$ and $T^{\mathrm{a}}_{\min}$ are the historical maximum and minimum atmospheric temperatures, respectively

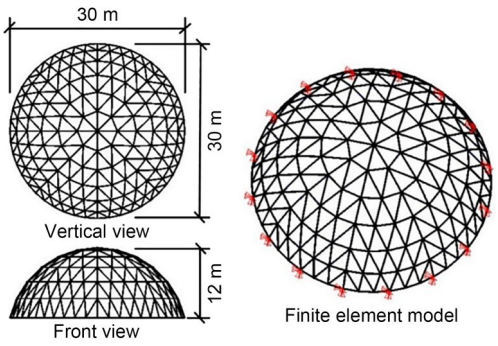

Fig. 21 Finite element model for structural analysis

member stress and nodal displacement were 44.6 MPa and 7.3 mm, reaching 14.4% and 9.7% of the design strength and deformation, respectively; under non-uniform thermal loads, the maximum member stresses reached 53.8, 73.0, and 70.1 MPa, while the maximum nodal displacements were 8.8, 11.1, and 11.3 mm, at healing times of 9:00, 12:00, and 15:00, respectively. Uniform thermal effects were much stronger than non-uniform ones, with a maximum increment of more than 60%. This implies that non-uniform thermal loads enable a more comprehensive analysis of structural thermal effects, preventing potential safety hazards.

4.2 Influence of healing time on non-uniform thermal effect

Table 6 shows that the selected healing time directly influences the structural thermal effect. To study this impact, we used 8760 h of healing time (24×365) from 2021 to analyze thermal effects. Fig. 22 shows the variation curves of the maximum member stress and nodal displacement under non-uniform temperature-rise loads (S^{r}_{max} and D^{r}_{max}), and maximum member stress and nodal displacement under non-uniform temperature-drop loads (S^{d}_{max} and D^{d}_{max}) for healing times on Mar. 1. As the peak and trough temperature fields were established, the positive and negative temperature differences depended solely on the healing temperature field. At nighttime, since the healing temperature field was uniformly below the AT, the positive temperature difference exceeded the negative one, making the temperature-rise effect more prominent. In the daytime, the environmental boundary conditions directly affected the healing temperature field. First, as solar radiation strengthened, the healing temperature field rose unevenly and the positive and negative

Table 6 Uniform and non-uniform thermal effects

Load type	Healing time	Maximum member stress (MPa)	Maximum nodal displacement (mm)
UTRL	–	44.6	7.3
UTDL	–	44.6	7.3
NTRL	9:00, Mar. 1	53.8	8.8
	12:00, Mar. 1	47.1	7.6
	15:00, Mar. 1	42.1	5.8
NTDL	9:00, Mar. 1	44.5	6.8
	12:00, Mar. 1	73.0	11.1
	15:00, Mar. 1	70.1	11.3

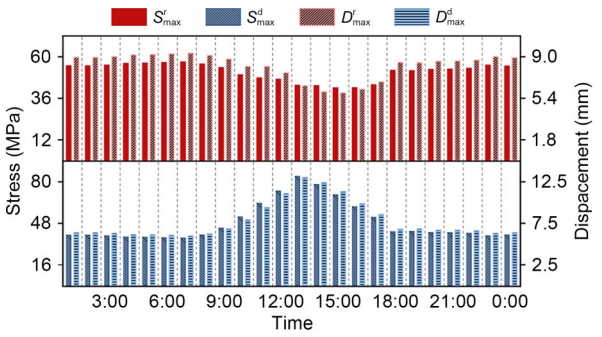

Fig. 22 Variations of non-uniform thermal effects for healing times on Mar. 1

temperature differences decreased and increased, respectively, making the enhanced temperature-drop effect stronger than the weakened temperature-rise effect; then, the healing temperature field peaked when the temperature-drop and temperature-rise effects were at their maximum and minimum, respectively; finally, with the weakening of solar radiation, the healing temperature field dropped non-uniformly and the positive and negative temperature differences became larger and smaller, respectively; thus the temperature-drop effect diminished and eventually became weaker than the progressively increasing temperature-rise effect. S^{r}_{max} and D^{r}_{max} peaked at 57.1 MPa and 9.3 mm at 7:00, while maximums of S^{d}_{max} and D^{d}_{max} reached 84.3 MPa and 13.0 mm at 13:00. The results indicate that the temperature-drop load was the thermal control load on Mar. 1, and healing construction should avoid times with significant temperature-drop effects.

Fig. 23 presents the variation curves of daily maximums of S^{r}_{max}, S^{d}_{max}, D^{r}_{max}, and D^{d}_{max} for healing times in 2021. The time-variant trends for daily maximums of

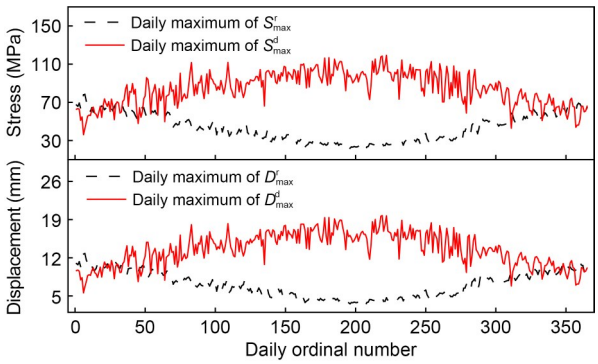

Fig. 23 Variation curves of non-uniform thermal effects for healing times in 2021

S^r_{max} and D^r_{max} followed a fluctuating pattern of initial rise and subsequent fall, which is almost the exact inverse of the patterns seen for daily maximums of S^d_{max} and D^d_{max}. On Jan. 7, the daily maximums of S^r_{max} and D^r_{max} peaked at 78.4 MPa and 12.8 mm, while those of S^d_{max} and D^d_{max} peaked at 119.3 MPa and 19.7 mm on Aug. 10 and Aug. 7, respectively. The maximum member stress and nodal displacement under non-uniform thermal loads (119.3 MPa and 19.7 mm) were 267.5% and 269.9%, respectively, of those under uniform thermal loads (44.6 MPa and 7.3 mm). In addition, the non-uniform thermal effects exhibited notable seasonal variations in their change processes. Table 7 presents the non-uniform thermal effects corresponding to the four seasons and indicates that thermal effects were the most severe during summer healing days and the least intense during winter ones. Hence, it is advisable to schedule healing time in winter and avoid it in summer. Temperature-drop loads appear to be the thermal control loads for most heating days throughout the year, barring a few winter days. For healing days governed by temperature-rise loads, the most adverse thermal effects typically occurred at night, when the healing temperature field was at its daily minimum. Therefore, it is recommended to schedule healing at midday, when the healing temperature field reaches its daily maximum. For the same reasons, for healing days controlled by temperature-drop loads, we suggest arranging the healing time at nighttime, when the healing temperature field is at its daily low. The healing construction recommendations are summarized as follows:

1. Determine healing date: it is recommended to schedule the healing date during winter and avoid it in summer.

2. Determine healing time: for healing dates governed by temperature-rise loads, midday is the optimal time for healing, while for dates controlled by temperature-drop loads, healing is best scheduled at nighttime.

5 Conclusions

In this study, we investigated the non-uniform thermal behavior of a single-layer spherical reticulated shell via numerical analysis, theoretical derivation, and experiments, and we proposed a design method for non-uniform thermal loading. Some conclusions can be drawn as follows:

1. Using a systematic numerical method and considering practical environmental boundary conditions, shadow variations, and the dynamic coupling effect of environmental factors, long-term temperature changes in a single-layer spherical reticulated shell were simulated. The non-uniform distribution characteristics and time-variant regularity of the structure's temperature field were analyzed from the perspective of seasonal and daily variations.

2. By integrating numerical analysis results, a simplified design method for non-uniform thermal loads of single-layer spherical reticulated shells was proposed via theoretical derivation. The method effectively evaluates the impacts of time-varying environmental factors like non-uniform solar and longwave radiation absorption, and convective heat transfer between the structure and flowing air, on the structure's temperature field.

Table 7 Non-uniform thermal effects for healing times in the four seasons

Season	Daily maximum of S^r_{max} (MPa)		Daily maximum of S^d_{max} (MPa)		Daily maximum of D^r_{max} (mm)		Daily maximum of D^d_{max} (mm)	
	Average	Maximum	Average	Maximum	Average	Maximum	Average	Maximum
Spring	42.5	59.7	88.2	111.8	6.9	9.7	14.4	18.3
Summer	27.0	36.1	100.5	119.3	4.4	5.9	16.5	19.7
Autumn	43.5	62.4	82.5	112.7	7.1	10.2	13.1	18.4
Winter	62.1	78.4	65.6	95.8	10.1	12.8	10.2	14.9

3. Verification experiments revealed a maximum temperature difference of 6.1 ℃ and a maximum error rate of 9.7% between the calculated and tested results. The distribution patterns of simulated and calculated temperature fields align, with the deviations not exceeding 6.0 ℃. Through comparative analysis, the design method's accuracy and reliability were validated, and its application was demonstrated in several cases.

4. The design method was employed to examine non-uniform thermal effects on a single-layer spherical reticulated shell. Under non-uniform thermal loads, the maximum member stress and nodal displacement reach 119.3 MPa and 19.7 mm, respectively, with an increase of 167.5% and 169.9% compared to uniform loads. Furthermore, the impacts of healing construction time on non-uniform thermal effects were assessed, leading to construction recommendations.

Acknowledgments

This work is supported by the National Natural Science Foundation of China (Nos. 51578491 and 52238001).

Author contributions

Wucheng XU designed the research and wrote the first draft of the manuscript. Xiaoqing ZHENG supervised and administrated the project. Xuanhe ZHANG and Zhejie LAI helped to organize the manuscript. Yanbin SHEN revised and edited the final version.

Conflict of interest

Wucheng XU, Xiaoqing ZHENG, Xuanhe ZHANG, Zhejie LAI, and Yanbin SHEN declare that they have no conflict of interest.

References

Chen DS, Qian HL, Wang HJ, et al., 2017a. Non-uniform temperature field measurement and simulation of a radio telescope's main reflector under solar radiation. *Applied Thermal Engineering*, 111:1330-1341. https://doi.org/10.1016/j.applthermaleng.2016.10.032

Chen DS, Wang HJ, Qian HL, et al., 2017b. Experimental and numerical investigation of temperature effects on steel members due to solar radiation. *Applied Thermal Engineering*, 127:696-704. https://doi.org/10.1016/j.applthermaleng.2017.08.045

Chen DS, Xu WC, Qian HL, et al., 2020. Effects of non-uniform temperature on closure construction of spatial truss structure. *Journal of Building Engineering*, 32:101532. https://doi.org/10.1016/j.jobe.2020.101532

Chen DS, Xu WC, Qian HL, et al., 2021. Thermal behavior of beam string structure: experimental study and numerical analysis. *Journal of Building Engineering*, 40:102724. https://doi.org/10.1016/j.jobe.2021.102724

Deng XS, Tang ZA, 2011. Moving surface spline interpolation based on Green's function. *Mathematical Geosciences*, 43(6):663-680. https://doi.org/10.1007/s11004-011-9346-5

Fan F, Jin XF, Shen SZ, 2009. Effect of non-uniform solar temperature field on cable-net structure of reflector of large radio telescope-FAST. *Advances in Structural Engineering*, 12(4):503-512. https://doi.org/10.1260/136943309789508447

GMAO (Global Modeling and Assimilation Office), 2015. MERRA-2 inst1_2d_asm_Nx: 2d, 1-Hourly, Instantaneous, Single-Level, Assimilation, Single-Level Diagnostics V5.12.4 (M2I1NXASM). GMAO. https://disc.gsfc.nasa.gov/datasets/M2I1NXASM_5.12.4/summary

Greve A, Bremer M, 2010. Thermal Design and Thermal Behaviour of Radio Telescopes and Their Enclosures. Springer, Berlin, Germany, p.173-261. https://doi.org/10.1007/978-3-642-03867-9

Greve A, Karcher HJ, 2009. Performance improvement of a flexible telescope through metrology and active control. *Proceedings of the IEEE*, 97(8):1412-1420. https://doi.org/10.1109/JPROC.2009.2013566

Hottel HC, 1976. A simple model for estimating the transmittance of direct solar radiation through clear atmospheres. *Solar Energy*, 18(2):129-134. https://doi.org/10.1016/0038-092X(76)90045-1

Kim SH, Park SJ, Wu JX, et al., 2015. Temperature variation in steel box girders of cable-stayed bridges during construction. *Journal of Constructional Steel Research*, 112:80-92. https://doi.org/10.1016/j.jcsr.2015.04.016

Liu HB, Chen ZH, 2016. Non-Uniform Temperature Effect of Solar Radiation on Long-Span Structures. Science Press, Beijing, China, p.34-127 (in Chinese).

Liu HB, Chen ZH, Zhou T, 2012a. Numerical and experimental investigation on the temperature distribution of steel tubes under solar radiation. *Structural Engineering and Mechanics*, 43(6):725-737. https://doi.org/10.12989/sem.2012.43.6.725

Liu HB, Chen ZH, Zhou T, 2012b. Theoretical and experimental study on the temperature distribution of H-shaped steel members under solar radiation. *Applied Thermal Engineering*, 37:329-335. https://doi.org/10.1016/j.applthermaleng.2011.11.045

Liu HB, Chen ZH, Han QH, et al., 2014. Study on the thermal behavior of aluminum reticulated shell structures considering solar radiation. *Thin-Walled Structures*, 85:15-24. https://doi.org/10.1016/j.tws.2014.07.007

Liu HB, Liao XW, Chen ZH, et al., 2015. Thermal behavior of spatial structures under solar irradiation. *Applied Thermal Engineering*, 87:328-335. https://doi.org/10.1016/j.applthermaleng.2015.04.079

MOHURD (Ministry of Housing and Urban-Rural Development of the People's Republic of China), 2010. Technical Specification for Space Frame Structures, JGJ 7–2010. National Standards of the People's Republic of China

(in Chinese).

MOHURD (Ministry of Housing and Urban-Rural Development of the People's Republic of China), 2012. Load Code for the Design of Building Structures, GB 50009–2012. National Standards of the People's Republic of China (in Chinese).

Qian HL, Chen DS, Fan F, et al., 2016. Evaluation of solar temperature field under different wind speeds for Shanghai 65 m radio telescope. *International Journal of Steel Structures*, 16(2):383-393. https://doi.org/10.1007/s13296-016-6011-3

Xia Y, Chen B, Zhou XQ, et al., 2013. Field monitoring and numerical analysis of Tsing Ma Suspension Bridge temperature behavior. *Structural Control and Health Monitoring*, 20(4): 560-575. https://doi.org/10.1002/stc.515

Xu WC, Chen DS, Qian HL, 2020. Non-uniform temperature fields and effects of steel structures: review and outlook. *Applied Sciences*, 10(15):5255. https://doi.org/10.3390/app10155255

Xu WC, Chen DS, Qian HL, et al., 2021. Non-uniform temperature field and effects of large-span spatial truss structure under construction: field monitoring and numerical analysis. *Structures*, 29:416-426. https://doi.org/10.1016/j.istruc.2020.11.014

Zhao ZW, Liu HB, Chen ZH, 2017. Thermal behavior of large-span reticulated domes covered by ETFE membrane roofs under solar radiation. *Thin-Walled Structures*, 115:1-11. https://doi.org/10.1016/j.tws.2017.01.025

Zhou M, Fan JS, Liu YF, et al., 2020. Non-uniform temperature field and effect on construction of large-span steel structures. *Automation in Construction*, 119:103339. https://doi.org/10.1016/j.autcon.2020.103339

Zhou Y, Sun LM, 2019. A comprehensive study of the thermal response of a long-span cable-stayed bridge: from monitoring phenomena to underlying mechanisms. *Mechanical Systems and Signal Processing*, 124:330-348. https://doi.org/10.1016/j.ymssp.2019.01.026